SSRG International Journal of Electronics and Communication Engineering
ISSN: 2348-8549/ https://doi.org/10.14445/23488549/IJECE-V12I7P102

Volume 12 Issue 7, 13-23, July 2025

Original Article

Advancements in Brain Tumor Detection using Transfer Learning Model with CNN-based Multi-Head Attention for Tumor Type Classification

V. Chanemougavel[1], K. Jayanthi[2]

[1]*Department of Computer Science, Arignar Anna Govt Arts & Science College, Nehru Nagar, Karaikal, Puducherry, India.*
[2]*Department of Computer Applications, Government Arts College, C. Mutlur, Chidambaram, Tamil Nadu, India.*

[1]*Corresponding Author : vchvel@gmail.com*

Received: 01 May 2025 Revised: 03 June 2025 Accepted: 02 July 2025 Published: 31 July 2025

Abstract *- Brain Tumour (BT) is a common and aggressive disorder that leads to a very short life expectancy in high-grade grades. Therefore, treatment planning is the primary phase in enhancing the quality of patient care. Numerous image models like Computed Tomography (CT), ultrasound imaging, and Magnetic Resonance Imaging (MRI) were employed to assess a brain's cancer region. Compared to other image techniques, MRI images are used to analyze the tumour in the brain. Conversely, the enormous amount of data generated by MRI scans prevents the manual classification of non-tumours and tumours in a precise manner. However, it is time-consuming and requires knowledge to examine the MRI imaging. Currently, the development of Computer-Aided Diagnosis (CAD), Machine Learning (ML), and Deep Learning (DL) models permits the expert to recognize BT. This manuscript presents a Hybrid Artificial Intelligence-Based Brain Tumor Classification with Transfer Learning and Metaheuristic Optimization (HAIBTC-TLMO) model using MRI imaging. The HAIBTC-TLMO model aims to develop an effective and accurate method for classifying BTs. Image pre-processing begins with noise removal using a bilateral filter (BF), followed by skull removal through Otsu thresholding and morphological operations. Moreover, the proposed HAIBTC-TLMO model utilizes the NASNetMobile method for feature extraction to detect the BT region from the input image data. The hybrid Graph Convolutional Gated Recurrent Network (GCGRN) method is also employed for classification. Finally, the Spotted Hyena Optimizer (SHO) optimally adjusts the hyperparameters of the GCGRN method, resulting in improved classification performance. The experimental analysis of the HAIBTC-TLMO approach is conducted on a BT MRI dataset. The performance validation of the HAIBTC-TLMO approach demonstrated a superior accuracy output of 94.64% over existing methods.*

Keywords *- Artificial Intelligence, Brain tumor classification, Transfer learning, Metaheuristic optimization, MRI.*

1. Introduction

The brain is the control centre and a crucial part of the nervous system for regulating daily activities [1]. It receives signals or stimuli from the body's sensory organs and processes them to make choices, sending commands to the muscles. BT represent a critical condition where abnormal brain cells grow uncontrollably, leading to a disorder [2]. It is possible for virtually any person of any age. It can even change from one therapy period to another, but its causes cannot be the same for any person [3]. BT appears in different images at different locations and intensities and is of various sizes and shapes. BT of low-level is named as benign. Likewise, the high level is called malignant [4]. Benign cancer is not a tumorous cancer. Therefore, the brain does not spread to other parts. Nevertheless, the malignant tumour is cancerous. Consequently, it spreads fast with unpredictable borders to different zones of the body [5]. It also causes direct death. Treatment of BT utilizes many approaches. Nevertheless, MRI is selected over other imaging methods, namely Positron Emission Tomography (PET), CT, and X-rays, because it has no interfering features [6]. MRI is recognized as a robust and efficient technique for visualizing the brain, allowing continuous tracking over longitudinal, non-invasive, and 3D assessment of soft tissue morphology, function, physiology, and metabolism [7]. MRI's data has seriously grown the information of standard and health research on disorder anatomy and is the main section in diagnosis and planning treatment. MRI is the prevalent method for the early detection of BT.

The traditional system of brain MRI identification and human inspection treatment is tumour detection, including MRI, which is affected by the operation implementation and can cause serious mistakes in classification. The MRI information is obtained via a vast, natural, complex cognitive process. Perfect MRI data analysis demands more time and is

not a simple procedure. Therefore, the literature survey has announced semi-automatic and automatic methods for the BT division. Semi-automatic approaches need human intervention for BT recognition [8]. Trained radiologists perform judgment tasks with considerable accuracy. For diagnostic ability and excellent accuracy in the pathological classification of brain tissues, Computer-Aided Diagnosis (CAD) systems are presented, which can produce diagnosis reports depending on MRI and guide the radiologist [9]. The CAD method has developed dramatically by applying DL and ML applications in the health check imaging area [10]. Such techniques result in better precision in identifying BT in the CAD system. Swift BT detection significantly enhances patient outcomes and guides effective treatment strategies. Conventional diagnostic methods often face difficulty with tumour size, shape, and location variability across individuals. Advanced DL approaches can improve diagnostic precision through automated image analysis. Transfer Learning (TL) and Attention Mechanisms (AM) can improve tumour classification performance, even with limited annotated data.

This manuscript presents a Hybrid Artificial Intelligence-Based Brain Tumor Classification with Transfer Learning and Metaheuristic Optimization (HAIBTC-TLMO) model using MRI imaging. The HAIBTC-TLMO model aims to develop an effective and accurate method for classifying BTs. Image pre-processing begins with noise removal using a Bilateral Filter (BF), followed by skull removal through Otsu thresholding and morphological operations. Moreover, the proposed HAIBTC-TLMO model utilizes the NASNetMobile method for feature extraction to detect the BT region from the input image data. The hybrid graph Convolutional Gated Recurrent Network (GCGRN) method is also employed for classification. Finally, the Spotted Hyena Optimizer (SHO) optimally adjusts the hyperparameters of the GCGRN method, resulting in improved classification performance. The experimental analysis of the HAIBTC-TLMO approach is conducted on a BT MRI dataset. The major contribution of the HAIBTC-TLMO approach is listed below.

- The HAIBTC-TLMO model utilizes the BF model for noise reduction while conserving critical edges, enhancing the clarity of MRI images. It improves tumour localization through precise skull removal utilizing Otsu thresholding and morphological operations.
- The HAIBTC-TLMO method employs the NASNetMobile technique for extracting deep, discriminative features from brain MRI scans, capturing complex tumour characteristics. This improves its capability to distinguish between diverse tumour types accurately.
- The HAIBTC-TLMO approach implements the hybrid GCGRN model to effectively capture spatial and sequential patterns in feature representations from MRI scans. This strengthens the model's classification accuracy across various tumor types.
- The HAIBTC-TLMO methodology integrates the SHO model to fine-tune parameters, enabling faster convergence during training. This results in improved performance and stability across classification tasks.
- The HAIBTC-TLMO model presents a novel unified model incorporating BF-based pre-processing, NASNetMobile-based feature extraction, and GCGRN-based classification. It also includes the SHO method for parameter tuning and optimizing learning efficiency. This novel approach improves both tumour classification accuracy and computational performance.

2. Related Works

In [11], an automated model deploying a Particle Swarm Optimizer (PSO) is implemented to generate a CNN structure mainly improved for the classification of MRI-based BT. PSO is scientifically searching for an optimum configuration of structural parameters. Abdusalomov et al. [12] combine YOLO-v5, an advanced structure of OD, with a Non-Local Neural Network (NLNN) model. This paper begins by organizing a complete database, including brain MRI scans from several resources. The NLNN and YOLO-v5, SPPF+, and K-means+ models were combined inside a unified structure to assist effective fusion. The BT database upgrades the YOLO-v5 technique over applying the TL models. In [13], a fast and precise BTSC method was advanced depending upon a TL-based Convolutional Neural Network (CNN). The images are partitioned by utilizing the VGG-19 method. Afterwards, the final classified output was attained from the adapted VGG-19 framework. Kumaar et al. [14] developed an innovative model that employs an auxiliary classification of BT and a style-based generative adversarial network. An open-source MRI database supported the presented model. Sachdeva and Kushwaha [15] developed an AI-based automated structure to categorize tumours. The given structure leverages the hierarchical feature learning ability of the CNN model and an enhanced boosting technique. Hyperparameters of the boosting classifier are adjusted with a Bayesian optimizer.

Ramakrishnan et al. [16] project a hybrid CNN structure applying VGG16, Inception-V3, DenseNet, and ResNet-50. Primarily, this model eliminates characteristics from MRI images and subsequently categorizes the tumour utilizing the mask image, which is later incorporated with the original image. Lastly, the resultant image is categorized using diverse CNN methods, particularly VGG16, Inception-V3, DenseNet, and ResNet. Kumar et al. [17] introduce an advanced structure for the classification of BT, incorporating XGBoost for classification and EfficientNet-B0 for feature extraction. The pre-processing phase contains normalization, resizing, and data augmentation of brain MRI pictures to guarantee high-quality input. The parameter efficacy and computational speed of the EfficientNet-B0 model are employed to remove discriminative characteristics, which are categorized utilizing the XGBoost model. Global Average Pooling and a dropout ratio of 0.3 methods were used. Tariq et al. [18] propose a DL

methodology using EfficientNetV2 for effectual feature extraction and a Vision Transformer (ViT) for capturing global context in brain tumour classification. Sajol and Hasan [19] explore seven advanced models, comprising transformer-based and self-attention replicating architectures, for BT classification utilizing MRI scans.

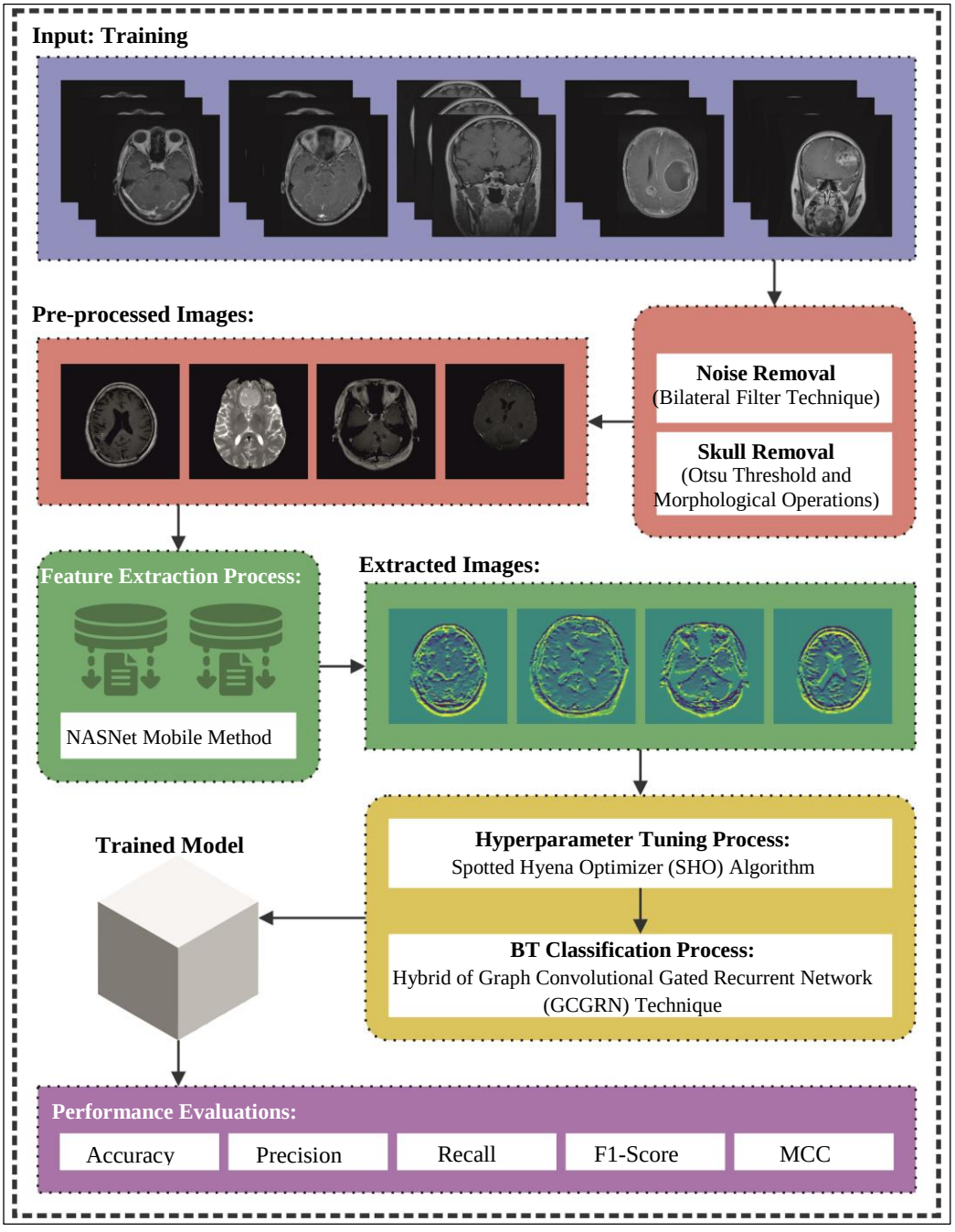

Fig. 1 Overall flow of HAIBTC-TLMO model

Wang et al. [20] introduce MSegNet, a Transformer-based segmentation model incorporating cross-modal attention and multi-view approach. The method comprises three data augmentation methods to improve robustness and generalization. Lai et al. [21] explore pre-trained models for BT classification, concentrating on the novel Vision Mamba (Vim) architecture. The method also utilizes TL methods for the tuning process. Li and Zhou [22] present a BT MRI classification model with a dual-branch structure: ResNet50 with a Multi-Head Self-Attention (MHSA) model for global context and VGG16 for local features. An attention-enhanced fusion module combines features, and a category attention

block addresses class imbalance. Pacal et al. [23] present an improved EfficientNetv2 model with Global AM (GAM) and Efficient Channel Attention (ECA), improving feature extraction and classification accuracy. Preetha, Priyadarsini, and Nisha [24] propose a three-branch CNN with EfficientNetB2 fusion for multiclass BT classification, outperforming existing multi-branch architectures. Srinivas et al. [25] introduce a fine-tuned transformer model integrating a data-efficient image transformer (DeiT) and the Firefly algorithm (FA) technique for BT classification. The model utilizes self-attention and hyperparameter optimization to capture intrinsic patterns in MRI images.

Despite crucial improvements in BT classification using diverse DL models, there remains a research gap in attaining consistent high accuracy across diverse MRI datasets due to variability in tumour types and imaging conditions. High computational costs and inadequate generalization across diverse data sources limit several existing techniques. Furthermore, while AMs and transformers have exhibited superiority, their application in BT classification is still under-explored, specifically in integrating multimodal data for enhanced robustness. Enhancing model interpretability and mitigating overfitting in small datasets are also critical challenges.

3. Methodology

This manuscript proposes the HAIBTC-TLMO technique using MRI imaging. The method aims to classify BTs. To perform that, the HAIBTC-TLMO model comprises pre-processing, feature engineering, BT-based classification, and parameter tuning. Figure 1 signifies the complete flow of the HAIBTC-TLMO model.

3.1. Image Pre-Processing

First, the BF model removes noise and skulls using the Otsu threshold and morphological operations.

3.1.1. BF for Noise Removal

Bilateral is a nonlinear filter that preserves edges and smooth images [26]. Compared with conventional convolutional filters, it utilizes various kernels to calculate proximity in intensity areas. BF represents a weighted average of neighbouring pixels.

$$I_p = \frac{1}{W_p}\sum_{q\in s} G_{\sigma_s}\left(\|\|p-q\|\|\right)G_{\sigma_r}\left(\|I_p - I_q\|\right)I_q \qquad (1)$$

Whereas (W_p) is the normalization feature that is delineated as shown:

$$W_p = \sum_{q\in s} G_{\sigma_s}\left(\|p-q\|\right)G_{\sigma_r}\left(\|I_p - I_q\|\right)I_q \qquad (2)$$

The parameters σ_s and σ_s state the filtering level applied to the image (I). If (q) pixels' intensity values may vary (I_p), the Gaussian range G_{σ_s} lessens their effect. G_{σ_s} refers to the Gaussian weight applied to reduce the distant pixel effects.

3.2. Skull Removal

3.2.1. Otsu Threshold

This is used for segmenting the denoised images for BT [27]. This approach employs between-class variation as a criterion to determine the optimal threshold. This value that maximizes the difference among class labels is the optimal threshold. Assume L signifies the complete amount of diverse grey levels and n_i symbolizes the complete pixel counts using the grey level value i. When the pixel's grey levels in the image $f(x,y)$ range from 0 to L-l.

$$N = \sum_{i=0}^{L=1} n_i \qquad (3)$$

The frequency designated is applied to estimate the possibility of the pixel having a grey level value, i, whereas p_i denotes probability.

$$p_i = \frac{n_i}{N} \qquad (4)$$

When T is applied as the threshold value for binary segmentation, the pixels of the image are separated into two classes, selected as c_0 and c_1. In contrast, c_0 and c_1 correspondingly represent pixel groups with pixels with grey values in $[0,T]$ and $[T+1, L\text{-}l]$. There is a limited critical statistic, which is required to be involved before the interclass variance is described, comprising the value of the mean pixel grey c_0 and c_1, in addition to the weighting parameters that are decided individually as symbols $\mu_0(T), \mu 0_0(T), \mu_0(T)$.

3.2.2. Morphological Operations

The morphological processes of erosion, dilation, closing, opening, thickening, and thinning are applied, correspondingly, to divide the images and eliminate smaller objects by making a disk-shaped structuring component with a radius of 8 that relies on the skull, tumour, and image size [28]. A similar size is selected for each image; therefore, attaining the best number of disks is simpler. The radius value is significant because it verifies the size of the disk-shaped structuring component and successively influences how much of the image is measured to be a portion of the object to be removed. A large radius leads to a significant structuring component and might eliminate more objects than projected. However, a small radius gives a small structuring component and can leave some items behind. To establish a suitable radius for a particular image, dissimilar radii are verified to discover the one that best eliminates the object while preserving a significant amount of the neighbouring tissue as promising. This might include running the object removal model numerous times with dissimilar radii and comparing the outcomes to verify which gives the best result. Finally, while a radius of 8 is recommended as a starting point, the particular

value of the disk-shaped structuring component must be selected according to the features of the pending image. Now, the opening operator displays more precise outcomes for tumour area computation.

3.3. Feature Extraction

Moreover, the proposed HAIBTC-TLMO model implements the NASNetMobile methodology to extract the feature process to remove the BT region from the input image data. The NASNetMobile methodology is a mobile-optimized Neural Network (NN) structure for image classification tailored to the neural structure [29]. It attains advanced precision on ImageNet classification amongst mobile-sized methods. This study presents a NASNet searching region, which allows effective framework search on a smaller dataset, namely CIFAR-10, and transmits the learned framework to larger-scale difficulties such as ImageNet classification. The search model utilizes a control RNN that samples child network structures that are trained and estimated. It captures a static 224x224 input image, which initially passes through Stem convolutional layers for the initial feature extraction. The Stem supports stacked modular blocks named cells consisting of dual categories: (1) Normal Cells to take spatial features over processes such as 1x1, 3x3 pooling, skip connections, and convolutions; and (2) Reduction Cells to decrease the width and height of features through extensive pooling and convolutions. Consecutive intermediary convolution layers then process features, previously global average pooling shortens the outputs for the last classification layer, usually comprising as many neurons as classes. NASNetMobile hit a good spot for precision efficacy calculated for embedded uses, exceeding hand-designed methods. Figure 2 depicts the NASNetMobile model.

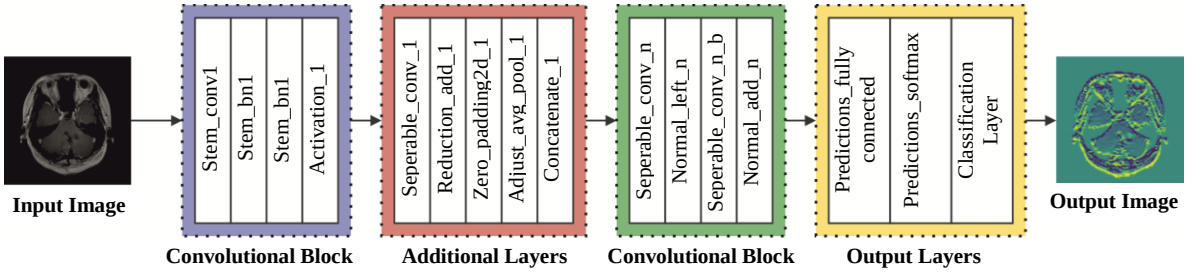

Fig. 2 Framework of NASNetMobile

3.4. BT Classification Model

The hybrid of the GCGRN technique is employed for the BT classification model. GCN is an NN structure specified for graph-structured data [30]. The graph-structured data contains edges and nodes that connect pairs of nodes. Compared with sequence, graph, and grid-structured data, the inter-relationships among nodes can be explained by using edges. The undirected graph is typically stated as shown:

$$\begin{cases} G = (V, E, X, A) \\ V = (v_0, v_1, \dots, v_N) \\ E = (v_i, v_j), G \text{ is an undirected graph} \end{cases} \quad (5)$$

Whereas signified by V represents a set of nodes using N nodes, represented by E denotes edge collection, $X \in \Re^{N \times d}$ characterizes the node's feature matrix by d dimension attributes, and $A \in R^{N \times N}$ refers to the matrix of weight adjacency. The nodes might characterize the sensors' measuring point and the edges' weighting.

The GCN is made by streamlining spectral graph convolutions using a first-order calculation. Therefore, they first briefly analyze the spectral graph convolutions. Assume $G = (V, E, X, A)$ denotes an undirected graph; the matrix of standardized Laplacian of G was provided by:

$$L = I_N - D^{-\frac{1}{2}} A D^{\frac{1}{2}} \quad (6)$$

On the other hand, $D = di(lg(\sum_j A_{ij})$ denotes the degree matrix of G, and I_N refers to a matrix of identity.
The eigenvalue decomposition of L is expressed as:

$$L = U \Lambda U^T \quad (7)$$

Here, Λ denotes the eigenvalues diagonal matrix, U represents the eigenvectors matrix, and T characterizes the transpose operator. Formerly, the spectral graph convolution was described as:

$$h = g_\theta \star X = U g_\theta U^T X \quad (8)$$

Now, h denotes feature mapping after graph convolution, $U^T X$ signifies the graph Fourier transform of X, $\star$ denoting the operator of the graph convolution, and $g_\theta = diag(\theta)$ characterizes filters within the Fourier field parameterized by $\theta \in \Re^N$ that is assumed as the function of Λ, for example, $g_\theta(\Lambda)$.

$$g_{\theta'}(\Lambda) \approx \sum_{k=0}^{K} \theta'_k \, T_k(\tilde{\Lambda}) \quad (9)$$

Whereas $T_k(x) = 2xT_{k-1}(x) - T_{k-2}(x)$ with $T_0(x) = 1$ and $T_1(x) = x$, $\tilde{\Lambda} = \frac{2}{\lambda_{max}}\Lambda - I_N$ and $\lambda_{\max}$ epitomizes the larger eigenvalues of L. Formerly, the convolution of the graph was provided by:

$$h = g_{\theta'} \star X = \sum_{k=0}^{K} \theta'_k T_k(\tilde{L})X \quad (10)$$

with $\tilde{L} = \frac{2}{\lambda_{max}}L - I_N$. As it solely relies on the Kth neighbourhood order.

Afterwards, the function of nonlinear activation, the GCN using only the message passed stage, is described as:

$$H^{(l+1)} = \sigma\left(D^{-\frac{1}{2}}AD^{-\frac{1}{2}}H^{(l)}W_1^{(l)} + H^{(l)}W_0^{(l)} + b^{(l)}\right) \quad (11)$$

Whereas represented by $H^{(l)} \in \Re^{N\times d_l}(H^{(0)} = X$, for example, the input node feature matrix denotes a hidden node representation matrix with dimensions d_l within the lth layer. σ denotes the activation function of ReLU. $W_0^{(l)} \in \Re^{d_l\times d_{l+1}}$ and $W_l \in \Re^{d_l\times d_{l+1}}$ they are learnable parameter matrices. b signifies a biased vector. $D^{-1/2}AD^{-1/2}$ denote the matrix of the standardized adjacency. To additionally lower the parameters of the model, the only GCN parameter method in $the\ lth$ layer was provided by:

$$H^{(l+1)} = \sigma\left(\tilde{D}^{-\frac{1}{2}}\tilde{A}\tilde{D}^{-1/2}H^{(l)}W_V^{(l)} + b^{(l)}\right) \quad (12)$$

Here, $\tilde{A} = A + I_N, \tilde{D}^{-1/2}\tilde{A}\tilde{D}^{-1/2}$ characterizes the matrix of standardized adjacency with additional self-connections and $\tilde{D}_{ii} = \sum_j \tilde{A}_{ij}$. $W^{(l)} \in \Re^{d_l\times d_{l+1}}$ IT is the matrix of learnable parameters. The difficulty of the particular GCN is $O(N^2 d_l + N d_l d_{l+1})$.

LSTM and GRU are two popular RNN versions extensively applied to model temporal dependencies in time series. The forward propagation at instant t is provided by:

$$r_t = \sigma(W_r x_t + V_r h_{t-1} + b_r) \quad (13)$$

$$u_t = \sigma(W_u x_t + V_u h_{t-1} + b_u) \quad (14)$$

$$\tilde{h}_t = \tanh(W_h x_t + V_h(r_t \odot h_{r-1}) + b_h) \quad (15)$$

$$h_t = u_t \odot h_{t-1} + (1 - u_t) \odot \tilde{h}_t \quad (16)$$

Here, $\odot$ characterizes the Hadamard product. $r_t \in \Re^{d_h\times 1}$ signifies the reset gate. $u_t \in \Re^{d_h\times 1}$ denotes the update gate.

$x_t \in \Re^{d_x\times 1}$ epitomizes the present input. $h_{t-1} \in \Re^{d_h\times 1}$ and $h_t \in \Re^{d_h\times 1}$ embody the preceding and present hidden layer (HL). $\tilde{h}_t \in \Re^{d_h\times 1}$ refers to candidate HL. d_x and d_h represent the sizes of x_t and h_{t-1} individually. $\{W_r, W_u, W_h\} \in \Re^{d_h\times d_x}$ and $\{V_r, V_u, V_h\} \in \Re^{d_h\times d_h}$ denotes weighting matrices to x_t and h_{t-1}, correspondingly. $\{b_r, b_u, b_h\} \in \Re^{d_h\times 1}$ symbolizes biased vectors. σ stands for the function of sigmoid activation. $tanh$ refers to the function of hyperbolic tangent activation. The core concept of the GRU comprises update and reset gates that control how much data from the previous hidden state is retained and how much of the current input is passed to the output, addressing the gradient vanishing issue in RNNs and handling time dependencies in sequences.

3.5. SHO-based Parameter Tuning

Finally, the SHO approach optimally alters the hyperparameter value of the GCGRN model and results in better classification performance. The SHO model is a meta-heuristic optimizer model developed by the social hierarchy and searching actions of spotted hyenas [31]. This model simulates the cooperative searching tactics and social communications noted in Hyena, which effectively resolve optimizer problems. Naturally, spotted hyenas search in crowds and show an intricate social hierarchy. In the same way, during SHO, the optimizer procedure is influenced by the candidate solution's population, which is observed as a group of members. Hyenas work together throughout searches, utilizing tactics like coordinated attacks, cooperative hunting, and information sharing. During SHO, these behaviours transform into information exchange amongst individual hyenas (candidate solutions) to improve the exploitation and exploration of the searching region. Inside a hyena group, leading individuals frequently guide and organize the group's movements. During SHO, leading roles are allocated to capable leaders (solutions) that lead the exploitation and exploration stages.

The pre-defined target function evaluates all candidates' solutions' fitness, which states the solution quality regarding the optimizer issue. This estimation defines the achievement of the candidate solution (Hyena) within the optimizer procedure. This model repeats over numerous groups (epochs), whereas candidate solutions develop and adjust according to their communications and the supervision of leaders. The model remains until an ending condition is encountered, like a maximum number of solution reiterations to the satisfaction level. The following series of equations characterize the surrounding activities in the SHO. (17) & (18).

$$\vec{X}_h = \left|\vec{A} \cdot \vec{C}_p(X) - \vec{C}(X)\right| \quad (17)$$

$$\vec{C}(X+1) = \vec{C}_p(X) - \vec{B} \cdot \vec{X}_h \quad (18)$$

The distance covered by the spotted Hyena to the admission of its target is represented as $\vec{X}_h$. The present iteration is specified by x. $\vec{C}$ and $\vec{C}_p$ individually represent position vectors for the spotted Hyena and the victim. The symbols || and · denote absolute values and multiplication

vectors. The vectors of coefficients $\vec{A}$ and $\vec{B}$ are calculated as shown:

$$\vec{A} = 2 \cdot \vec{x}\, \vec{d}_1 \tag{19}$$

$$\vec{A} = 2 \cdot \vec{h} \cdot \vec{d}_2 - \vec{h} \tag{20}$$

$$\vec{h} = 5 - \left(\frac{Itr \times 5}{\mathrm{Max}_{ltr}}\right) \tag{21}$$

Whereas $itr = 0,1,2 \ldots., \mathrm{Max}_{ltr}$

The $\vec{h}$ value reduces from (5-0) during all iterations. The randomly formed vectors $x\,\vec{d}_1$ and $x\,\vec{d}_2$ capture values in intervals of $(0,1)$. Changing the position vectors $\vec{A}$ and $\vec{B}$ allows the exploration of dissimilar locations. In addition, by utilizing the succeeding equations, the hyenas' searching behaviours are replicated, permitting the recognition of possible searching areas.

$$\vec{X}_h = \left|\vec{A} \cdot \vec{C}_h - \vec{C}_k\right| \tag{22}$$

$$\vec{C}_k = \vec{C}_h - \vec{B} \cdot \vec{X}_h \tag{23}$$

$$\vec{O}_h = \vec{C}_k + \vec{C}_{k+1} + \cdots, + \vec{C}_{k+N} \tag{24}$$

N refers to iteration counts that are measured as demonstrated:

$$N = Count_{nos}\left(\vec{C}_h, \vec{C}_{h+1}, \vec{C}_{h+2}, \cdots, \vec{C}_{h+M}\right) \tag{25}$$

$$\vec{C}(X+1) = \frac{\vec{O}_h}{N} \tag{26}$$

The operational stage of the SHO model originates after the size of $\vec{B}$ is lower than one, and it is randomly initialized in the interval of [-1, 1]. During the process of SHO, the optimizer procedure starts by making a population of arbitrary solutions. Primarily, the searching agents group together by enlightening the locations of the best-performing agents and then fine-tuning their locations. During all iterations, the features h and E linearly reduce. After the iteration is effectively finished, the optimal locations related to the searching agents are recovered.

Fitness selection is a crucial aspect that influences the accomplishment of the SHO approach. The hyperparameter range process involves a solution-encoded system used to evaluate the efficiency of candidate outputs. In the SHO method, accuracy is the primary criterion for determining the fitness function. Its mathematical model is given below:

$$Fitness = \max(P) \tag{27}$$

$$P = \frac{TP}{TP + FP} \tag{28}$$

Meanwhile, FP and TP signify the positive values of false and true.

4. Performance Validation

The analysis of the HAIBTC-TLMO technique is investigated under the BT MRI dataset [32]. This dataset holds 7013 counts under dual classes, such as non-cancerous and cancerous, as depicted in Table 1. Figure 3 explains the sample images. Figure 4 demonstrates the pre-processing and extraction images.

Table 1. Dataset specification

Classes	Images Count
Non-Cancerous	5392
Cancerous	1621
Total Count	**7013**

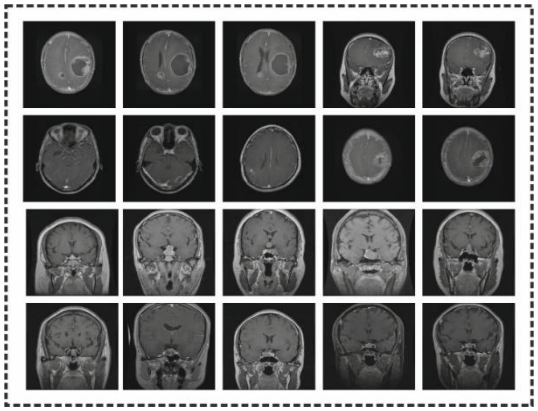

Fig. 3 Sample images

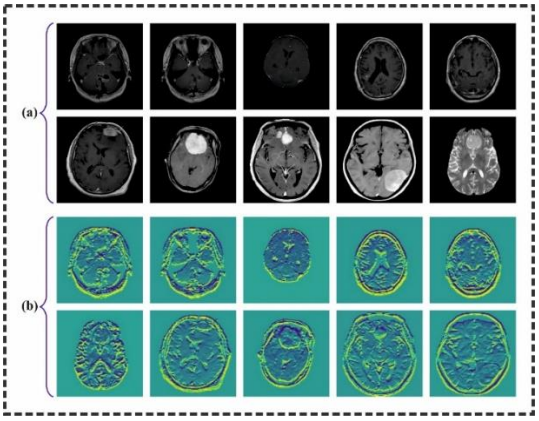

Fig. 4 (a) Pre-processed image, and (b) Extracted image.

Figure 5 exhibits the classifier outputs of the HAIBTC-TLMO technique under 70%TRAPHA. Figure 5(a) presents the confusion matrix with the precise classification and identification of overall classes. Figure 5(b) denotes the PR curve, notifying the maximal outcome through all class labels. Eventually, Figure 5(c) represents the ROC inspection and establishes competent outputs with higher ROC values for several classes.

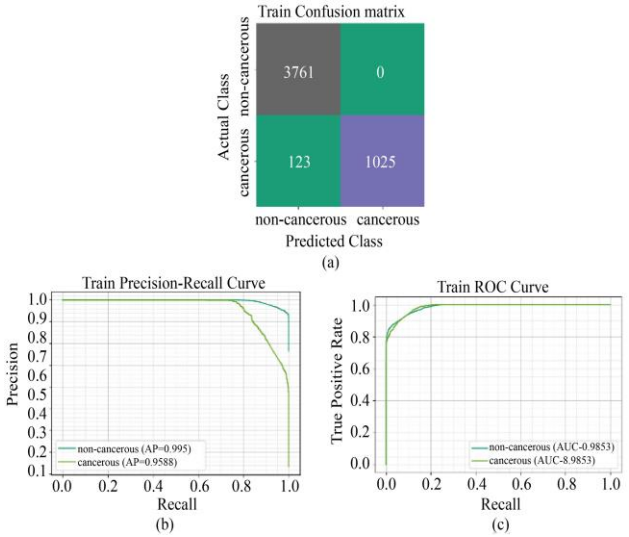

Fig. 5 TRAPHA 70% (a) confusion matrix, and (b) PR and ROC curves.

Figure 6 exhibits the classifier outputs of the HAIBTC-TLMO method under 30%TESPHA. Figure 6(a) illustrates the confusion matrix with precise classification and detection of every class. Figure 6(b) illustrates the PR examination, designating the highest values across both class labels. Ultimately, Figure 6(c) illuminates the study of ROC, exemplifying effective outputs with extraordinary ROC for diverse classes.

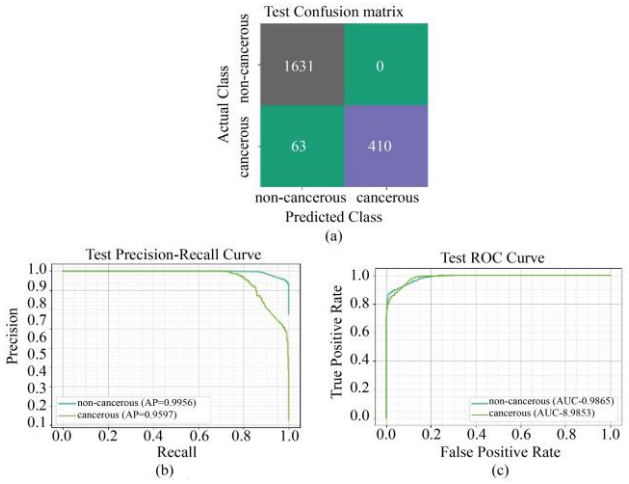

Fig. 6 TESPHA 30% (a) confusion matrix, and (b) PR and ROC curves.

Table 2 and Figure 7 indicate the BT detection of the HAIBTC-TLMO technique on 70%TRAPHA and 30%TESPHA. The results recommend that the HAIBTC-TLMO technique accurately identifies the samples. With 70%TRAPHA, the HAIBTC-TLMO model presents average $accu_y$, $prec_n$, $reca_l$, $F1_{score}$, and MCC of 94.64%, 98.42%, 94.64%, 96.36%, and 92.98%, individually. Moreover, with 30%TESPHA, the HAIBTC-TLMO model provides average $accu_y$, $prec_n$, $reca_l$, $F1_{score}$, and MCC of 93.34%, 98.14%, 93.34%, 95.49%, and 91.35%, correspondingly.

Table 2. BT detection of HAIBTC-TLMO model under 70%TRAPHA and 30%TESPHA

Class	$Accu_y$	$Prec_n$	$Reca_l$	$F1_{score}$	MCC
TRAPHA (70%)					
Non-Cancerous	94.64	96.83	100.00	98.39	92.98
Cancerous	94.64	100.00	89.29	94.34	92.98
Average	**94.64**	**98.42**	**94.64**	**96.36**	**92.98**
TESPHA (30%)					
Non-Cancerous	93.34	96.28	100.00	98.11	91.35
Cancerous	93.34	100.00	86.68	92.87	91.35
Average	**93.34**	**98.14**	**93.34**	**95.49**	**91.35**

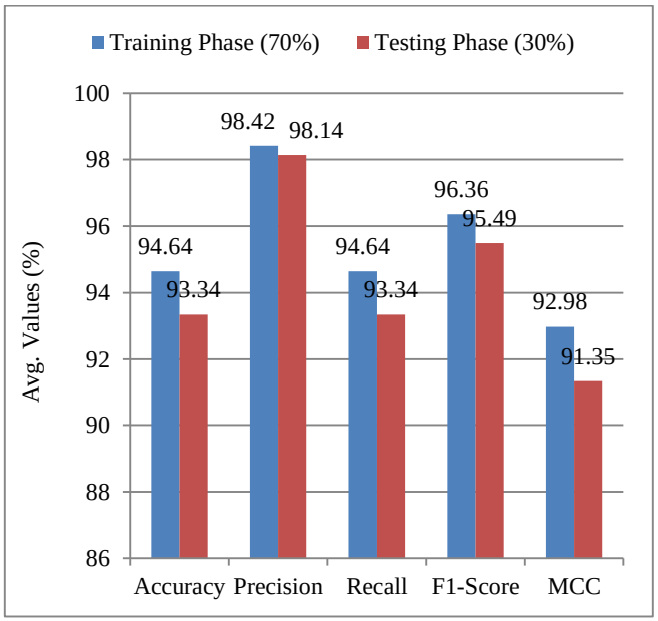

Fig. 7 Average of HAIBTC-TLMO model under 70%TRAPHA and 30%TESPHA

Figure 8 depicts the TRAN $accu_y$ and VALN $accu_y$ outcomes of the HAIBTC-TLMO approach. The $accu_y$ values are calculated within an interval of 0-200 epochs. The TRAN and VALN $accu_y$ values consistently increase, highlighting the improved performance of the HAIBTC-TLMO approach across iterations. Additionally, their proximity over epochs shows reduced overfitting, illustrating the enhanced performance and reliability of the model in predicting unseen samples.

Figure 9 illustrates the TRANLOS and VALNLOS graph of the HAIBTC-TLMO approach. Loss values are computed over 0-200 epochs, with TRANLOS and VALNLOS depicting a decreasing trend. This demonstrates the capability of the HAIBTC-TLMO approach to balance generalization and data fitting. The continuous reduction in loss values portrays improved performance and prediction outputs.

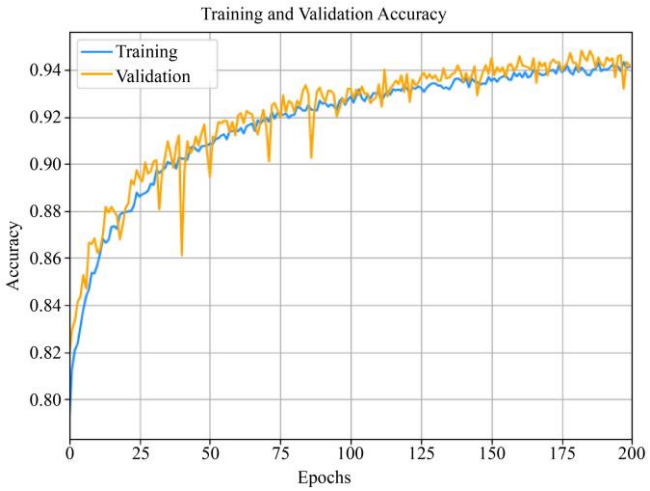

Fig. 8 $Accu_y$ curve of HAIBTC-TLMO model

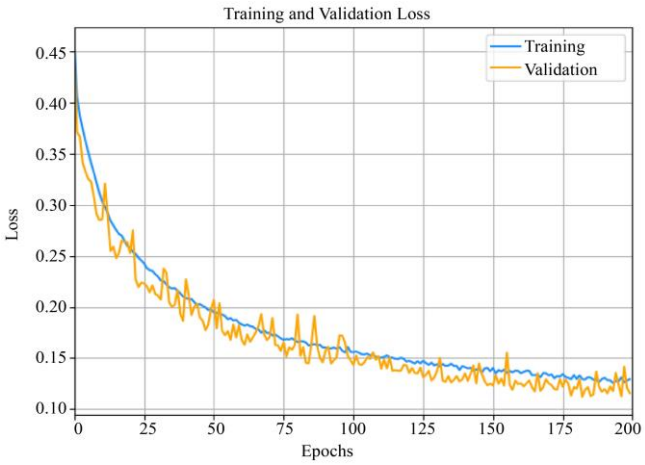

Fig. 9 Loss curve of HAIBTC-TLMO model

Table 3. Comparison evaluation of HAIBTC-TLMO approach with existing models [33-35]

Approach	$Accu_y$	$Prec_n$	$Reca_l$	$F1_{score}$	Time (sec)
K-NN	85.00	90.35	89.40	94.78	13.30
SOM Model	92.00	89.04	91.66	93.89	21.14
U-Net-DenseNet	88.70	97.39	92.72	88.06	18.87
LeUNet	93.55	92.59	88.26	91.82	10.54
Xception Model	93.97	97.52	93.50	94.82	25.68
VGG16 Method	92.20	89.06	89.38	94.99	13.01
ResNet152v2	90.78	91.43	88.81	91.40	12.16
HAIBTC-TLMO	94.64	98.42	94.64	96.36	08.61

Table 3 and Figure 10 compare the HAIBTC-TLMO model with existing models [33-35] under different measures. The outputs underlined that the K-NN, SOM, U-Net-DenseNet, LeUNet, Xception, VGG16, and ResNet152v2 methods have gained poor performance.

However, the presented HAIBTC-TLMO approach obtained better performance with maximal $accu_y, prec_n$, $reca_l$ and $F1_{score}$ of 94.64%, 98.42%, 94.64%, and 96.36%, individually.

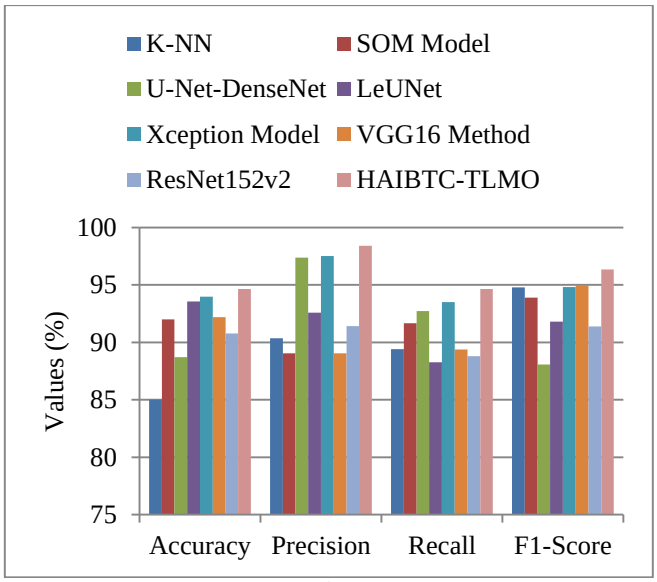

Fig. 10 Comparison evaluation of HAIBTC-TLMO approach with existing models

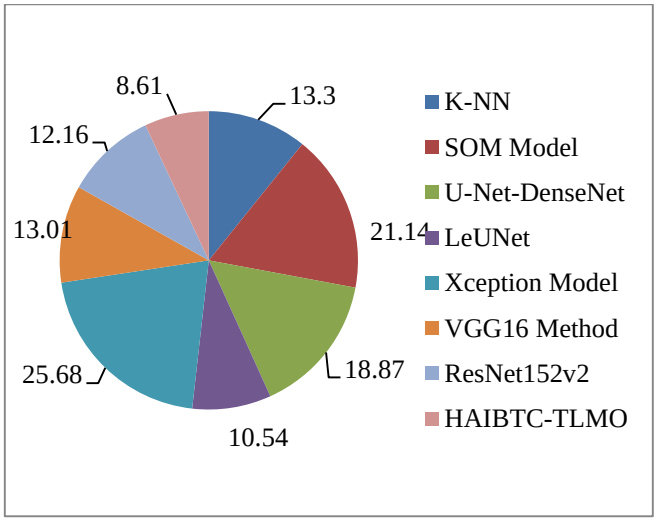

Fig. 11 Time outcome of HAIBTC-TLMO technique with existing models

Figure 11 presents the timely results of the HAIBTC-TLMO methodology with recent techniques. According to time, the HAIBTC-TLMO methodology attains a lower time of 08.61sec; however, the K-NN, SOM, U-Net-DenseNet, LeUNet, Xception, VGG16, and ResNet152v2 approaches reach superior times of 13.30sec, 21.14sec, 18.87sec, 10.54sec, 25.68sec, 13.01sec, and 12.16sec, respectively.

5. Conclusion

In this manuscript, the HAIBTC-TLMO approach using MRI imaging is proposed. The HAIBTC-TLMO approach aims to develop an effective and accurate method for classifying BTs. The image pre-processing stage initially utilizes BF for noise and skull removal using the Otsu threshold and morphological operations. Moreover, the proposed HAIBTC-TLMO approach implements the NASNetMobile method for feature extraction. The hybrid of the GCGRN technique is employed for BT classification. Finally, the SHO method is implemented for tuning. The experimental analysis of the HAIBTC-TLMO approach is conducted on a BT MRI dataset. The performance validation of the HAIBTC-TLMO approach demonstrated a superior accuracy output of 94.64% over existing methods.

References

[1] Nyoman Abiwinanda et al., "Brain Tumor Classification Using Convolutional Neural Network," *World Congress on Medical Physics and Biomedical Engineering 2018, Prague*, Czech Republic, vol. 1, pp. 183-189, 2018. [CrossRef] [Google Scholar] [Publisher Link]

[2] Wadhah Ayadi et al., "Deep CNN for Brain Tumor Classification," *Neural Processing Letters*, vol. 53, pp. 671-700, 2021. [CrossRef] [Google Scholar] [Publisher Link]

[3] Ahmad Saleh, Rozana Sukaik, and Samy S. Abu-Naser, "Brain Tumor Classification Using Deep Learning," *2020 International Conference on Assistive and Rehabilitation Technologies*, Gaza, Palestine, pp. 131-136, 2020. [CrossRef] [Google Scholar] [Publisher Link]

[4] Asaf Raza et al., "A Hybrid Deep Learning-Based Approach for Brain Tumor Classification," *Electronics*, vol. 11, no. 7, pp. 1-17, 2022. [CrossRef] [Google Scholar] [Publisher Link]

[5] Hassan Ali Khan et al., "Brain Tumor Classification in MRI Image Using Convolutional Neural Network," *Mathematical Biosciences and Engineering*, vol. 17, no. 5, pp. 6203-6216, 2020. [CrossRef] [Google Scholar] [Publisher Link]

[6] Dillip Ranjan Nayak et al., "Brain Tumor Classification Using Dense Efficient-Net," *Axioms*, vol. 11, no. 1, pp. 1-13, 2022. [CrossRef] [Google Scholar] [Publisher Link]

[7] Muhammad Aamir et al., "A Deep Learning Approach for Brain Tumor Classification Using MRI Images," *Computers and Electrical Engineering*, vol. 101, 2022. [CrossRef] [Google Scholar] [Publisher Link]

[8] Isselmou Abd El Kader et al., "Differential Deep Convolutional Neural Network Model for Brain Tumor Classification," *Brain Sciences*, vol. 11, no. 3, pp. 1-16, 2021. [CrossRef] [Google Scholar] [Publisher Link]

[9] Osman Özkaraca et al., "Multiple Brain Tumor Classification with Dense CNN Architecture Using Brain MRI Images," *Life*, vol. 13, no. 2, pp. 1-16, 2023. [CrossRef] [Google Scholar] [Publisher Link]

[10] Ehsan khodadadi, S.K. Towfek, and Hussein Alkattan, "Brain Tumor Classification Using Convolutional Neural Network and Feature Extraction," *Fusion: Practice & Applications*, vol. 13, no. 2, pp. 34-41, 2023. [CrossRef] [Google Scholar] [Publisher Link]

[11] Sofia El Amoury, Youssef Smili, and Youssef Fakhri, "Design of an Optimal Convolutional Neural Network Architecture for MRI Brain Tumor Classification by Exploiting Particle Swarm Optimization," *Journal of Imaging*, vol. 11, no. 2, pp. 1-19, 2025. [CrossRef] [Google Scholar] [Publisher Link]

[12] Akmalbek Abdusalomov et al., "Enhancing Automated Brain Tumor Detection Accuracy Using Artificial Intelligence Approaches for Healthcare Environments," *Bioengineering*, vol. 11, no. 6, pp. 1-23, 2024. [CrossRef] [Google Scholar] [Publisher Link]

[13] A. Maria Nancy, and R. Maheswari, "Brain Tumor Segmentation and Classification Using Transfer Learning Based CNN Model with Model Agnostic Concept Interpretation," *Multimedia Tools and Applications*, vol. 84, pp. 2509-2538, 2025. [CrossRef] [Google Scholar] [Publisher Link]

[14] M. Akshay Kumaar et al., "Brain Tumor Classification Using a Pre-Trained Auxiliary Classifying Style-Based Generative Adversarial Network," *International Journal of Interactive Multimedia and Artificial Intelligence*, vol. 8, no. 6, pp. 101-111, 2024. [CrossRef] [Google Scholar] [Publisher Link]

[15] Chandni, Monika Sachdeva, and Alok Kumar Singh Kushwaha, "AI-Based Intelligent Hybrid Framework (BO-DenseXGB) for Multi-Classification of Brain Tumor Using MRI," *Image and Vision Computing*, vol. 154, 2025. [CrossRef] [Google Scholar] [Publisher Link]

[16] Akshay Bhuvaneswari Ramakrishnan et al., "Optimizing Brain Tumor Classification with Hybrid CNN Architecture: Balancing Accuracy and Efficiency through One API Optimization," *Informatics in Medicine Unlocked*, vol. 44, pp. 1-8, 2024. [CrossRef] [Google Scholar] [Publisher Link]

[17] Hemant Kumar et al., "A Hybrid EfficientNetB0-XGBoost Framework for Efficient Brain Tumor Classification Using MRI Images," *Internet of Everything, and Machine Learning*, pp. 519-534, 2025. [CrossRef] [Google Scholar] [Publisher Link]

[18] Anees Tariq et al., "Transforming Brain Tumor Detection Empowering Multi-Class Classification With Vision Transformers and EfficientNetV2," *IEEE Access*, vol. 13, pp. 63857-63876, 2025. [CrossRef] [Google Scholar] [Publisher Link]

[19] Md Saiful Islam Sajol, and A.S.M Jahid Hasan, "Benchmarking CNN and Cutting-Edge Transformer Models for Brain Tumor Classification Through Transfer Learning," *2024 IEEE 12th International Conference on Intelligent Systems*, pp. 1-6, 2024. [CrossRef] [Google Scholar] [Publisher Link]

[20] Yu Wang et al., "MSegNet: A Multi-View Coupled Cross-Modal Attention Model for Enhanced MRI Brain Tumor Segmentation," *International Journal of Computational Intelligence Systems*, vol. 18, pp. 1-32, 2025. [CrossRef] [Google Scholar] [Publisher Link]

[21] Yinyi Lai et al., "Advancing Efficient Brain Tumor Multi-Class Classification -- New Insights from the Vision Mamba Model in Transfer Learning," *Arxiv*, pp. 1-10, 2024. [CrossRef] [Google Scholar] [Publisher Link]

[22] Zhiyong Li, and Xinlian Zhou, "A Global-Local Parallel Dual-Branch Deep Learning Model with Attention-Enhanced Feature Fusion for Brain Tumor MRI Classification," *Computers, Materials & Continua*, vol. 83, no. 1, pp. 739-760, 2025. [CrossRef] [Google Scholar] [Publisher Link]

[23] Ishak Pacal et al., "Enhancing EfficientNetv2 with Global and Efficient Channel Attention Mechanisms for Accurate MRI-Based Brain Tumor Classification," *Cluster Computing*, vol. 27, pp. 11187-11212, 2024. [CrossRef] [Google Scholar] [Publisher Link]

[24] R. Preetha, M. Jasmine Pemeena Priyadarsini, and J.S. Nisha, "Hybrid 3B Net and EfficientNetB2 Model for Multiclass Brain Tumor Classification," *IEEE Access*, vol. 13, pp. 63465-63485, 2025. [CrossRef] [Google Scholar] [Publisher Link]

[25] B. Srinivas et al., "A Fine-Tuned Transformer Model for Brain Tumor Detection and Classification," *Multimedia Tools and Applications*, vol. 84, pp. 15597-15621, 2025. [CrossRef] [Google Scholar] [Publisher Link]

[26] Assma G. Jaber, and Mohammed A. Mohammed, "Using Statistical Non-Linear Filters for Gaussian Carina Nebula Image Denoising," *Journal of Al-Rafidain University College For Sciences*, vol. 56, no. 1, pp. 431-443, 2025. [CrossRef] [Google Scholar] [Publisher Link]

[27] M. Anlin Sahaya Infant Tinu, Ahilan Appathurai, and N. Muthukumaran, "Detection of Brain Tumour Via Reversing Hexagonal Feature Pattern for Classifying Double-Modal Brain Images," *IETE Journal of Research*, vol. 70, no. 8, pp. 7033-7043, 2024. [CrossRef] [Google Scholar] [Publisher Link]

[28] Marzieh Ghahramani, and Nabiollah Shiri, "An Adaptive Neuro-Fuzzy Inference System Optimized by Genetic Algorithm for Brain Tumour Detection in Magnetic Resonance Images," *IET Image Processing*, vol. 18, no. 5, pp. 1358-1372, 2024. [CrossRef] [Google Scholar] [Publisher Link]

[29] Farid et al., "Bangladeshi Vehicle Classification and Detection Using Deep Convolutional Neural Networks with Transfer Learning," *IEEE Access*, vol. 13, pp. 26429-26455, 2025. [CrossRef] [Google Scholar] [Publisher Link]

[30] Lei Wang et al., "A Gated Graph Convolutional Network with Multi-Sensor Signals for Remaining Useful Life Prediction," *Knowledge-Based Systems*, vol. 252, 2022. [CrossRef] [Google Scholar] [Publisher Link]

[31] Saleem Mohammad, and S.D. Sundarsingh Jeebaseelan, "Hybrid Sine Cosine and Spotted Hyena Based Chimp Optimization for PI Controller Tuning in Microgrids," *Scientific Reports*, vol. 14, no. 1, pp. 1-29, 2024. [CrossRef] [Google Scholar] [Publisher Link]

[32] Masoud Nickparvar, Brain Tumor MRI Dataset, Kaggle. [Online]. Available: https://www.kaggle.com/datasets/masoudnickparvar/brain-tumor-mri-dataset

[33] Abdullah A. Asiri et al., "Optimized Brain Tumor Detection: A Dual-Module Approach for MRI Image Enhancement and Tumor Classification," *IEEE Access*, vol. 12, pp. 42868-42887, 2024. [CrossRef] [Google Scholar] [Publisher Link]

[34] Karrar Neamah et al., "Brain Tumor Classification and Detection Based DL Models: A Systematic Review," *IEEE Access*, vol. 12, pp. 2517-2542, 2023. [CrossRef] [Google Scholar] [Publisher Link]

[35] Seoyoung Yoon, "Brain Tumor Classification Using a Hybrid Ensemble of Xception and Parallel Deep CNN Models," *Informatics in Medicine Unlocked*, vol. 54, pp. 1-8, 2025. [CrossRef] [Google Scholar] [Publisher Link]